Journal of Nuclear Medicine, published on June 14, 2018 as doi:10.2967/jnumed.118.207753

Dual-isotope Cryo-imaging Quantitative Autoradiography (CIQA): Investigating Antibody-Drug Conjugate Distribution and Payload Delivery Through Imaging

Authors: Ohad Ilovich[1*], Mohammed Qutaish[1*], Jacob Y Hesterman[1], Kelly Orcutt[1‡], Jack Hoppin[1], Ildiko Polyak[1], Marc Seaman[1], Adnan O. Abu-Yousif[2], Donna Cvet[2] and Daniel P. Bradley[2†]

Affiliations: [1]Invicro, LLC, Boston, MA, [2]Takeda Pharmaceuticals International Co., Cambridge, MA

‡ To whom correspondence should be addressed: E-mail: orcutt@invicro.com

* These authors contributed equally to this work

† Present address: Preclinical Imaging and Pharmacology, Biogen, 125 Broadway, Cambridge, MA

Keywords: Autoradiography, Antibody-drug conjugate, dual isotope

Running title: CIQA for ADC intratumoral distribution

Word count: 4,919

ABSTRACT

In vitro properties of antibody drug conjugates (ADCs) such as binding, internalization, and cytotoxicity are often well characterized prior to in vivo studies. Interpretation of in vivo studies could significantly be enhanced by molecular imaging tools. We present here a dual-isotope cryo-imaging quantitative autoradiography (CIQA) methodology combined with advanced 3D imaging and analysis allowing for the simultaneous study of both antibody and payload distribution in tissues of interest in a pre-clinical setting. **Methods:** TAK-264, an investigational anti-guanylyl cyclase C (GCC) targeting ADC was synthesized utilizing tritiated Monomethyl auristatin E (MMAE). The tritiated ADC was then conjugated to DTPA, labeled with indium-111 and evaluated *in vivo* in GCC-positive and GCC-negative tumor-bearing animals. **Results:** CIQA reveals the time course of drug release from ADC and its distribution into various tumor regions that are less accessible to the antibody. For GCC-positive tumors, a representative section obtained 96 hours post tracer injection showed only 0.8% of the voxels have co-localized signal versus over 15% of the voxels for a GCC-negative tumor section, suggesting successful and specific cleaving of the toxin in the antigen positive lesions. **Conclusions:** The combination of a veteran established autoradiography technology with advanced image analysis methodologies affords an experimental tool that can support detailed characterization of ADC tumor penetration and pharmacokinetics.

INTRODUCTION

Antibody-drug conjugates (ADCs) are targeted pharmaceuticals that are comprise of a tumor-targeting monoclonal antibody conjugated to a highly potent cytotoxic drug. This approach aims to assess the safety profile of highly potent drugs with limited tolerability (*1*,*2*). Conjugation to monoclonal antibodies exploits the specific binding of the antibody as a selective delivery mechanism. This process relies on a series of events including target binding, receptor-mediated cellular internalization, lysosomal processing of the ADC to release active drug, and drug action on cellular machinery (e.g. DNA or microtubule) (*3*–*5*). In addition to exerting cytotoxic effects on antigen-positive cells, the processed cytotoxic drug may also diffuse out and damage adjacent tumor cells resulting in a bystander effect.

The antibody-drug conjugate approach results in the payload (active drug) taking on the pharmacokinetic properties of the antibody. As such, ADCs encounter one of the major challenges of antibodies, heterogenous distribution (*6*). As ADC technologies have advanced, the ability of a payload to exert bystander effects has been an area of active research. Linker designs aimed to release metabolites that are potent and cell-permeable have been developed with the goal of enabling cytotoxicity in proximal cells and greater efficacy in tumors with heterogenous antigen expression and/or heterogeneous penetration of ADC.

Traditionally, mechanism and efficacy are characterized *in vitro* for most new ADCs (*7*–*9*) with subsequent *in vivo* characterizations focused on pharmacokinetic and pharmacodynamic profiling, efficacy studies, and gross & destructive measurements of payload concentrations using mass spectrometry *ex vivo*. These techniques, while informative, don't allow for quantitative visualization of the extent of tumor penetration achieved by the antibody and processed drug.

The use of *in vivo* molecular imaging modalities such as positron emission tomography combined with long-lived isotopes such as zirconium-89 has allowed researchers to non-invasively evaluate parameters such as specific and non-specific tumor uptake, target engagement and off-target accumulation in both pre-clinical and clinical settings (*10*). positron emission tomography imaging, however, is limited to a spatial resolution on the order of millimeters, precluding evaluation of intra-tumor distribution of antibody and drug conjugate. Matrix assisted laser desorption/ionization mass spectrometry is an emerging methodology for imaging the 3D distribution of drugs, peptide and proteins *ex vivo*. Despite its high resolution and versatility, it is hampered by the need for arduous optimization of sample preparation and acquisition for different molecules and tissues (*11*,*12*) and by its lower sensitivity towards larger proteins. Autoradiography is a longstanding method for evaluating the distribution of target proteins using radiolabeled ligands *ex vivo*. The main uses of autoradiography have been the study of changes in neurotransmitter receptors in brain tissue (*13–15*) and for absorption, distribution, metabolism, and excretion studies (*16*,*17*).

Cryo-imaging quantitative autoradiography (CIQA) is an imaging methodology which involved the autoradiographic analysis of sections throughout a tissue of interest to determine the intratissue distribution of a radiolabeled molecule of interest. The radiolabeling of molecules with isotopes of significantly different half-lives enables dual isotope imaging, assisting in understanding how the molecules interact/affect each other.

This study describes the development of CIQA combined with 3D modeling to evaluate the intra-tumoral distribution of both antibody and drug conjugate by using a dual-labeled ADC (^{111}In-DTPA-^{3}H-TAK-264). This technology opens a new door on understanding how an ADCs' dosing

and linker structure together with tumor vasculature and antigen expression affects drug distribution and efficacy.

MATERIALS AND METHODS

Radiochemistry

^{3}H-TAK-264 (17.6 MBq/4.5 mg) was buffer exchanged into HEPES buffer (0.1 M, pH 8.5) using an ultrafiltration tube (Amicon) and concentrated to approximately 5 mg/mL. Diethylenetriaminepentaacetic acid (DTPA) dianhydride in dimethyl sulfoxide (2 mg/mL) was added to the protein solution to obtain a DTPA:antibody molar ratio of 20:1, and the reaction incubated at 4 °C overnight. The reaction was buffer exchanged into ammonium acetate buffer (0.1 M, pH 6) and concentrated to approximately 5 mg/mL.

A solution of $^{111}InCl_3$ (8 µL, 300 MBq) was mixed with an equal volume of sodium acetate buffer (0.1M, pH 6). DTPA-^{3}H-TAK-264 (1.89 mg, 4.5 mg/mL) was added to the reaction mixture and the reaction diluted to 1 mL with additional ammonium acetate buffer (0.1 M, pH 6). The reaction mixture was left at room temperature for 30 minutes, was stopped by addition of a 10% (v/v) solution of ammonium acetate buffer (0.1 M, pH 6) containing 50 mM Ethylenediaminetetraacetic acid, and was incubated for a further 5 minutes at room temperature. The labeling solution was formulated by dilution with saline to a final volume of 2 mL. The final formulation was found have a radiochemical purity of 96.5% and specific activities of 296 MBq (^{111}In) and 7.4 MBq (^{3}H) per 1.89 mg of TAK-264 in 2 mL.

The affinities of the DTPA-conjugated antibodies to GCC was compared to that of the parent antibodies using enzyme-linked immunosorbent assay and was found to be similar (data not shown).

Animal Model

All animal studies were performed at the University of Massachusetts and at inviCRO with the approval of the University of Massachusetts Medical School and inviCRO Institutional Animal Care and Use Committees, respectively. Animals were kept at a temperature of 18-26 °C, a relative humidity of 50 ± 20% and intermittent light and dark cycles of 12 hours with food and water available *ad libitum*. Female SCID mice, 5-8 weeks old, were implanted with HEK-293 GCC#2 or HEK-293 cells (5×10^6 cell in 100% Matrigel) subcutaneously. Tumor xenografts were allowed to grow to 200-1500 mm^3 for imaging studies and 180-520 mm^3 for CIQA studies.

SPECT/CT Imaging

Animals were imaged on a NanoSPECT/CT (Bioscan, Inc.) utilizing a 9-pinhole aperture (1.4 mm diameter). Animals were imaged at 2 and 24 hours post-injection (20 minute scan with 50 seconds per projection each), 48 and 96 hours (24 minutes with 60 s/projection) and 144 hours (24-32 minutes with 60-80 seconds per projection). Scans were performed with a dual energy window (154-188 keV, 221-270 keV). Each single-photon emission computed tomography (SPECT) scan was followed by a computed tomography (CT) scan for anatomical reference (180 projections per rotation, 0.5 seconds per projection). Anesthesia during imaging was induced with 4-5% isoflurane and maintained with 1-2% isoflurane (0.5-1 L/min).

Tumor bearing animals HEK-293 GCC#2 (n=8) were split into two groups (n=4) according to tumor type, anesthetized and injected with either ^{111}In-DTPA-5F9 (19.8±0.55 MBq, n=4) or ^{111}In-TAK-264 (19.4±0.85 MBq, n=4) and imaged at the time points described above.

Biodistribution and Autoradiography

Tumor-bearing animals [HEK-293 (n=8) and HEK-293 GCC#2 (n=8)] were anesthetized and injected with 15.5 ± 0.6 MBq and 14.1 ± 1.4 MBq of ^{111}In-DTPA-^{3}H-TAK-264, respectively. Two animals from each group were sacrificed at each time point (1, 8, 24 and 96 hours post injection) and had their tumors resected. Upon resection, tumors were immediately blocked in 5% carboxymethyl-cellulose on crushed dry ice. ^{14}C-2-doxyglucose spiked India ink fiducials were inserted into the blocks which were then stored in a -20° C freezer. High-resolution optical images were acquired for each 30 µm section using a Canon EOS 70D camera and each tenth section was acquired, stored on 3M tape, dehydrated and exposed to phosphor image screens (GE Healthcare, BAS-SR) for 2-3 hours which were scanned using a BAS5000 image acquisition system to determine ^{111}In content.

^{3}H signal was overshadowed by signals of two components, (1) ^{111}In, and (2) long-lived radioactive contaminants in the $^{111}InCl_3$ used for labeling. The ^{111}In signal was removed by exploiting its faster physical decay compared to that of ^{3}H. In this study, ^{3}H signal was acquired after a delay of more than ten ^{111}In half-lives. The long-lived radioactive contaminants were gamma emitters which pass aluminum foil while the ^{3}H beta radiation does not. Thus, the contaminating signal was acquired by covering the tumor sections and quantification standards with a single layer of aluminum foil. This signal was subtracted from the "contaminated ^{3}H" signal

acquired without aluminum foil. ^{3}H acquisitions were done by exposure to tritium plates (GE Healthcare, BAS IP TR 2025) for 5 days.

Image Analysis – SPECT/CT

SPECT images were reconstructed using a scanner manufacturer-provided multi-pinhole OSEM algorithm. Regions of interest were delineated and quantified by manual fitting of constant-volume volumes of interested to the heart (243 mm^3), liver (143 mm^3), spleen (75 mm^3), left and right kidneys (500 mm^3) and muscle (50 mm^3) using VivoQuant (inviCRO, Boston, MA). Tumor regions of interest (130-1600 mm^3) were drawn manually and maximized to the size of the lesion. Non-tumor regions of interest volumes were fitted based on CT data and centered on the peak-of activity profile.

Image Analysis – Autoradiography

Autoradiography image analysis was performed using VivoQuant (inviCRO, Boston, MA). Individual white light (WL) images were aligned into a 3D data set using a fiducial based registration approach. First, ink/^{14}C fiducial centers within each slice image were detected by applying a normalized cross correlation with a disc image. Then, a rigid body transformation was estimated to align these images to a reference image. Least squared distance error was used as the optimization parameter for estimating the registration parameters. After registration, variation in intensity throughout the image stack was corrected for by a histogram-based color matching algorithm (*18*) to complete the final 3D WL data set.

^{111}In and ^{3}H autoradiography images were intensity calibrated using a set of standards included in each plate. Linear regression yielded a plate-specific calibration parameter to convert intensity values into units of kBq/g. Reconstruction of ^{111}In tumor 3D volumes started by splitting the calibrated plates containing multiple tumor section into individual ones. Next, ink/^{14}C registration fiducials were detected using the same algorithm used in the WL fiducial detection algorithm. The fiducials were used to co-register the plates into a 2D stack. Since autoradiography images were captured every 10 WL slices, linear interpolation was performed to produce the final 3D autoradiography data set with isotropic voxel size. Fiducial centers from the WL stack and ^{111}In stack were used to register the WL volume to its corresponding ^{111}In volume using a Procrustes transformation that allows translation, rotation and scaling. Both volumes were resampled to 25 μm isotropic voxels.

After allowing two months for ^{111}In decay, the relative intensity of the ^{111}In standards (containing only contaminants, no measurable ^{111}In and no ^{3}H signal) in images on phosphor imaging screens with and without aluminum foil was used to estimate the contribution of the ^{111}In contaminants to ^{3}H signal in tumors. First, images of the standards acquired with and without foil were corrected for differences in exposure time. Next, a correction factor was calculated based on the relative intensity of the standards. This correction factor was used to scale the foil-covered (contaminant) image. After registering the two plates, the scaled, foil-covered image was smoothed with a Gaussian kernel of 0.1mm. Smoothing was used to preserve structure in the contaminant image while reducing the impact of noise. Finally, the scaled, smoothed contaminant image was subtracted from the image without foil to remove the signal contribution from the contaminants.

RESULTS

Generation of a Dual Labeled Antibody-Drug Conjugate – ^{111}In-DTPA-^{3}H-TAK-264

^{3}H-MMAE (185 MBq, 1 TBq/mmol, Moravek Biochemicals) was conjugated to the fully human anti-GCC monoclonal antibody, 5F9, via a protease-cleavable linker (MMAE and linker technology licensed from Seattle Genetics). The conjugate ^{3}H-TAK-264 was purified and formulated in 10mM histidine, 7.5% sucrose, 0.08% PS20, pH 5.2 to obtain 70.3 MBq of radiopharmaceutical with a radiochemical purity of 98.9%, specific activity of 3.9 MBq/mg and a drug to antibody ratio of 4.3:1.

^{3}H-TAK-264 was conjugated to DTPA, purified and formulated in ammonium acetate to give DTPA-^{3}H-TAK-264 with a DTPA:TAK-264 ratio of 0.9:1. DTPA-^{3}H-TAK-264 was labeled with pH buffered $^{111}InCl_3$ (Cardinal Health) with a labeling yield of >96% and was then formulated in saline to give ^{111}In-DTPA-^{3}H-TAK-264 with a ^{111}In radiochemical purity of 96.5% and specific activities of 311 MBq (^{111}In) and 7.4 MBq (^{3}H) per 1.89 mg of TAK-264 (155 KBq ^{111}In/µg TAK-264 and 3.7 KBq ^{3}H/µg TAK-264).

^{111}In-DTPA-5F9 and ^{111}In-DTPA-TAK-264 were prepared from 5F9 and TAK-264 using similar strategies for DTPA conjugation and indium-111 labeling as described for the dual labeled TAK-264. ^{111}In-DTPA-5F9 and ^{111}In-DTPA-TAK-264 were obtained in radiochemical purities of 98% and 93% and specific activities of 2.46 and 2.51 MBq/µg, respectively.

SPECT/CT was Used to Evaluate Tumor Accumulation Over Time for ^{111}In-DTPA-5F9 and ^{111}In-DTPA-TAK-264

^{111}In-DTPA-5F9 and ^{111}In-TAK-264 biodistribution profiles were evaluated via SPECT/CT imaging in mice bearing antigen positive tumors (HEK-293 GCC#2) at 2, 24, 48, 96 and 144h post injection (Supplemental Figs. 1 and 2). ^{111}In-DTPA-5F9 showed a continuous accumulation in tumors, averaging 16-18 %ID/g at 144 hours, ^{111}In-TAK-264 peak tumor uptake was reached at 96 hours post injection (11-13 %ID/g) and remained constant at 144 h post injection (Fig. 1). The differences in tumor uptake between ^{111}In-DTPA-5F9 and ^{111}In-TAK-264 are statistically significant in the first and last timepoints (2h and 144h with $p=0.015$ and $p=0.007$, respectively). Significant differences in plasma clearance (calculated based on the heart region of interest which approximates blood pool radioactivity) are apparent at ($p=0.03$).

Based on this data, the CIQA experiment was conducted on tumors resected at 1, 8, 24 and 96 hours post injection using the HEK-293 GCC#2 tumor model with the HEK-293 tumor as the antigen negative control.

CIQA Combined with 3D Image Reconstruction Used to Evaluate the Intra-Tumoral Distribution of Both 5F9 and its MMAE Payload

The original strategy for dual-isotope imaging consisted of quantifying the higher energy and shorter lived ^{111}In signal, allowing for sufficient ^{111}In decay (30 days, 11 half-lives), followed by quantification of the ^{3}H signal. The presence of small quantities (<0.1%) of long lived, gamma emitting isotope contaminants (^{114m}In and ^{65}Zn with half-lives of 50 and 244 days, respectively) necessitated an alternate quantitation strategy. After the ^{111}In signal had decayed to background the tissues were quantitated twice for radioactivity signal. First the total radioactive content (gamma emitting contaminants plus tritium) was quantitated by exposing tissues to standard phosphor imaging screens. Exposures were repeated with the screens covered in foil to block the

tritium signal, effectively quantitating contaminant signal only. Subtraction of the smoothed contaminant signal from the total signal yielded the tritium tissue signal.

Autoradiography sections for both ^{111}In and ^{3}H were co-registered to each other and to high resolution white light images to enable the analysis and correlation of information obtained with each isotope (Fig. 2). Three dimensional volumes of tumors were reconstructed by interpolating the gap between autoradiography sections and resampling at isotropic voxel size of 0.025 mm. Maximum intensity projections were used to visualize tumors in three dimensions (supplemental Fig. 3 is a diagram of the acquisition/reconstruction process; supplemental movie 1 shows the 3D reconstructed images).

CIQA Demonstrates Differential Distribution of MMAE in Antigen Negative and Antigen Positive Tumors

Representative tumor sections at 1, 24 and 96 hours post injection are shown in Fig. 3. At 1 hour and 8 hours (data not shown) post injection, ^{3}H and ^{111}In signals are very co-localized in both GCC-positive and antigen negative tumors (Fig. 3A). At 24 hours, ^{3}H and ^{111}In signals are still very co-localized in the antigen negative tumor, but are starting to diverge in the GCC-positive tumor (Fig. 3B). By 96 hours, ^{3}H and ^{111}In show a visible drop in signal intensity in the antigen negative tumors and exhibit some divergence (Fig. 3C). The GCC-positive tumor exhibits further divergence in ^{3}H and ^{111}In signals compared to 24 h with ^{3}H signal penetrating deeper into the tumor (Fig. 3C). Both tumor types demonstrate significant heterogeneity in the distribution of the antibody signal (^{111}In) as expected for large molecule weight compounds (*19*,*20*).

The ^{111}In signal in HEK-293 GCC#2 tumors steadily increases over the 96-hour period while ^{111}In signal in HEK-293 decreases as the non-specifically bound tracer is slowly washed out of the tumor (Fig. 4). A similar trend is clearly visible with the MMAE-affiliated ^{3}H signal with the main difference that the tritium signal spreads into the center of the HEK-293 GCC#2 tumors while the ^{111}In signal remains localized at the tumor edges.

Co-localization Analysis of ^{3}H and ^{111}In in GCC-positive and GCC-negative Tumors Demonstrates Bystander Affect

Differences in background and photon scatter characteristics in autoradioluminograms of the two isotopes can impact assessment of co-localization of the ^{111}In and ^{3}H signals (*21*). To improve pixel-by-pixel comparison between the two sets of autoradioluminograms, ^{3}H images were smoothed with a 2D, 150μm full width half maximum Gaussian kernel. Subsequent analysis of signal overlap focused on 1) differences in overall signal intensity between tumor lines and 2) the extent of co-localization of the ^{111}In and ^{3}H signals in the highest intensity voxels for each tumor line. The fraction of the highest intensity voxels that are common to both isotopes provides a measure of co-localization. Fig. 5 shows a 2D scatter plot of the thresholded voxels for tumors from each cell line at 96 hours. Threshold values in the HEK-293 GCC#2 tumors are 2-3 fold higher than those of the HEK-293 for both ^{111}In and ^{3}H. Additionally, these high intensity voxels are almost completely disparate between the two isotopes for HEK-293 GCC#2 (0.8% overlap) whereas a co-localization fraction of 15.5% is observed between the highest intensity voxels in the HEK-293 tumor (Supplementary Fig. 4 shows the same data without the thresholding). Taken together, this data demonstrates greater uptake of TAK-264 in HEK-293 GCC#2 xenograft tumors compared to antigen-negative HEK-293 tumors. In addition, the disparate signal observed between

the two isotopes in the GCC positive tumors is indicative of binding, internalization, metabolism, and release of MMAE.

DISCUSSION

Preliminary SPECT/CT imaging studies were performed on ^{111}In-labeled parent antibody and ADC to understand tissue distribution of the compounds over time. With the relevant distribution information at hand the ADC was dual-labeled with both ^{111}In (antibody) and ^{3}H (MMAE) and CIQA was performed in both HEK-293 GCC#2 (antigen positive) and HEK-293 (antigen negative) tumor-bearing animals at different times post injection.

Analysis of the highest intensity voxels allowed us to investigate the co-localization of both signals. For GCC-positive tumors, a representative section obtained 96 hours post tracer injection showed only 0.8% of the voxels have co-localized signal versus over 15% of the voxels for a GCC-negative tumor section. These results are in line with our expectation of antigen positive tumor cells internalizing and metabolizing the ADC, allowing for the free drug to diffuse across the tumor and affect untargeted cells in what is known as the "bystander effect" (*22*). In antigen-negative tumors, there is no target mediated internalization thus, a high percentage of co-localized signal is expected. Macropinocytosis has been shown to occur in response to growth factor stimulation and constitutively in some cell types and may cause of the decoupling of ^{111}In and ^{3}H signals observed in the antigen-negative tumors.

The indium contaminants made the CIQA process more difficult, time consuming and expensive than desired. A good companion isotope for ^{3}H/^{14}C would have a half-life of several days (matching well with the biological half-lives of antibodies yet enabling for a reasonable decay

period). The isotope of choice should residualize in tumors to minimize the redistribution of metabolites, emit low energy gamma energies to retain autoradiography resolution, have high specific activity and have short-lived contaminants. Gallium-67 is a residualizing isotope with established radiochemistry *(23–25)*, a half-life of 3.3 days, specific activity of 148 TBq/mmol, low energy gamma emissions and a minimal presence of short lived contaminants (<0.6%) of Gallium-66 and Gallium-68 with half-lives of 9.5 hours and 68 minutes, respectively. Its use as a surrogate for Indium-111 has been validated internally to ensure future CIQA studies will be more streamlined and cost effective.

The animals used in this study were not perfused prior to tumor harvesting. This was done to avoid potential translocation and loss of the MMAE due to the tissue handling (26). It is important to consider in the interpretation of the results that the tumor signal includes contributions both from tumor tissue and blood pool.

Although CIQA has some limitations such as the use of radioactive compounds, an inability to distinguish between the different radioactive metabolites and the need for extended periods of time to allow for radioisotope decay, it is well positioned when compared to imaging methodologies of similar scope. Fluorescence imaging is an inexpensive and straight forward methodology that allows for depth-limited *in vivo* imaging combined with superior *ex vivo* resolution. However, ADC conjugation to fluorescent dyes affects PK significantly even in low conjugate-to-antibody ratios (*27*) and the dyes themselves may undergo quenching following cellular uptake, making analysis challenging. Mass spectrometry imaging is a very attractive modality but it has two specific disadvantages. First, its detection sensitivity of large proteins over a tissue background is low. Second, as different metabolites will have different masses and may be conjugated to DNA/proteins, the signal may get more diluted over time and specific standards of the expected

metabolites would be required. Lastly, immunohistochemical identification of both drug conjugate and antibody are possible but require very specialized antibody pairs which may not have affinity to formed metabolites and produce signals that are more difficult to quantify.

CIQA is a unique and powerful method to evaluate the distribution and efficacy of antibody drug conjugates *in vivo*. CIQA allows the evaluation of ADC metabolism in tumors of varying antigen expression and organs (e.g., liver) known to have off target toxicities *(28)*. The results of this study are a proof of concept demonstrating that the CIQA technology can help understand the spatio-temporal dynamics of different antibodies, linkers and drug-conjugates.

ACKNOWLEDGMENTS: We are extremely grateful to the contributions of Vijay Gottumukkala, Paige Czarnecki, Mihaela Plesescu, Ozlem Yardibi, Rick Coelho, Merryl Lobo and Chris Graul for the execution and operationalizing of the study and the highly useful advice they shared.

DISCLOSURE: O.I., M.Q., J.H., K.O., J.H., I.P. and M.S. were all employed by Invicro LLC at the time experiments were conducted. A.O.A, D.C. and D.B. were all employed by Takeda Pharmaceuticals International at the time experiments were conducted.

REFERENCES

1. Blum RH, Wittenberg BK, Canellos GP, et al. A therapeutic trial of maytansine. *Cancer Clin Trials*. 1978;1:113-117.

2. Mirsalis JC, Schindler-Horvat J, Hill JR, Tomaszewski JE, Donohue SJ, Tyson CA. Toxicity of dolastatin 10 in mice, rats and dogs and its clinical relevance. *Cancer Chemother Pharmacol*. 1999;44:395-402.

3. Ducry L, Stump B. Antibody-drug conjugates: linking cytotoxic payloads to monoclonal antibodies. *Bioconjug Chem*. 2010;21:5-13.

4. Nolting B. Linker technologies for antibody-drug conjugates. *Methods Mol Biol*. 2013;1045:71-100.

5. Bareford LM, Swaan PW. Endocytic mechanisms for targeted drug delivery. *Adv Drug Deliv Rev*. 2007;59:748-758.

6. Thurber GM, Schmidt MM, Wittrup KD. Antibody tumor penetration: transport opposed by systemic and antigen-mediated clearance. *Adv Drug Deliv Rev*. 2008;60:1421.

7. Kularatne SA, Deshmukh V, Ma J, et al. A CXCR4-targeted site-specific antibody-drug conjugate. *Angew Chem Int Ed Engl*. 2014;53:11863-11867.

8. Tai Y-T, Mayes PA, Acharya C, et al. Novel anti-B-cell maturation antigen antibody-drug conjugate (GSK2857916) selectively induces killing of multiple myeloma. *Blood*. 2014;123:3128-3138.

9. Golfier S, Kopitz C, Kahnert A, et al. Anetumab ravtansine: a novel mesothelin-targeting antibody-drug conjugate cures tumors with heterogeneous target expression favored by

bystander effect. *Mol Cancer Ther*. 2014;13:1537-1548.

10. Lamberts LE, Williams SP, Terwisscha van Scheltinga AGT, et al. Antibody positron emission tomography imaging in anticancer drug development. *J Clin Oncol*. 2015;33:1491-1504.

11. Schwamborn K, Caprioli RM. MALDI imaging mass spectrometry--painting molecular pictures. *Mol Oncol*. 2010;4:529-538.

12. Quiason CM, Shahidi-Latham SK. Imaging MALDI MS of dosed brain tissues utilizing an alternative analyte pre-extraction approach. *J Am Soc Mass Spectrom*. 2015;26:967-973.

13. Kupila J, Karkkainen O, Laukkanen V, et al. [(3)H]Ifenprodil binding in post-mortem brains of Cloninger type 1 and 2 alcoholics: a whole-hemisphere autoradiography study. *Psychiatry Res*. 2015;231:197-201.

14. Yeh SH-H, Lin M-H, Kong F-L, et al. Evaluation of inhibitory effect of recreational drugs on dopaminergic terminal neuron by PET and whole-body autoradiography. *Biomed Res Int*. 2014;2014:157923.

15. Fang C-K, Chen H-W, Wang W-H, Liu R-S, Hwang J-J. Acute effects of three club drugs on the striatum of rats: evaluation by quantitative autoradiography with [18F]FDOPA. *Appl Radiat Isot*. 2013;77:153-159.

16. Solon EG. Autoradiography techniques and quantification of drug distribution. *Cell Tissue Res*. 2015;360:87-107.

17. Solon EG. Use of radioactive compounds and autoradiography to determine drug tissue distribution. *Chem Res Toxicol*. 2012;25:543-555.

18. Grundland M. Color histogram specification by histogram warping. *Proc SPIE*. 2005;5667:610-621.

19. Orcutt KD, Adams GP, Wu AM, et al. Molecular Simulation of Receptor Occupancy and Tumor Penetration of an Antibody and Smaller Scaffolds: Application to Molecular Imaging. *Mol Imaging Biol*. 2017;19:656-664.

20. Wilks MQ, Knowles SM, Wu AM, Huang S-C. Improved modeling of in vivo kinetics of slowly diffusing radiotracers for tumor imaging. *J Nucl Med*. 2014;55:1539-1544.

21. Johnston RF, Pickett SC, Barker DL. Autoradiography using storage phosphor technology. *Electrophoresis*. 1990;11:355-360.

22. Li F, Emmerton KK, Jonas M, et al. Intracellular released payload influences potency and bystander-killing effects of antibody-drug conjugates in preclinical models. *Cancer Res*. 2016;76:2710-2719.

23. Morais M, Cantante C, Gano L, et al. Biodistribution of a (67)Ga-labeled anti-TNF VHH single-domain antibody containing a bacterial albumin-binding domain (Zag). *Nucl Med Biol*. 2014;41 Suppl:e44-8.

24. Alirezapour B, R Jalilian A, Bolourinovin F, Moradkhani S. Production and quality control of [(67)Ga]-DOTA-trastuzumab for radioimmunoscintigraphy. *Iran J Pharm Res IJPR*. 2013;12:355-366.

25. Eder M, Knackmuss S, Le Gall F, et al. 68Ga-labelled recombinant antibody variants for immuno-PET imaging of solid tumours. *Eur J Nucl Med Mol Imaging*. 2010;37:1397-1407.

26. Walter SE. Drug localization in tissues and cells. Chapel Hill: IDDC-Press; 2003.

27. Cilliers C, Nessler I, Christodolu N, Thurber GM. Tracking Antibody Distribution with Near-Infrared Fluorescent Dyes: Impact of Dye Structure and Degree of Labeling on Plasma Clearance. *Mol Pharm*. 2017;14:1623-1633.

28. Gorovits B, Krinos-Fiorotti C. Proposed mechanism of off-target toxicity for antibody--drug conjugates driven by mannose receptor uptake. *Cancer Immunol Immunother*. 2013;62:217-223.

Figures

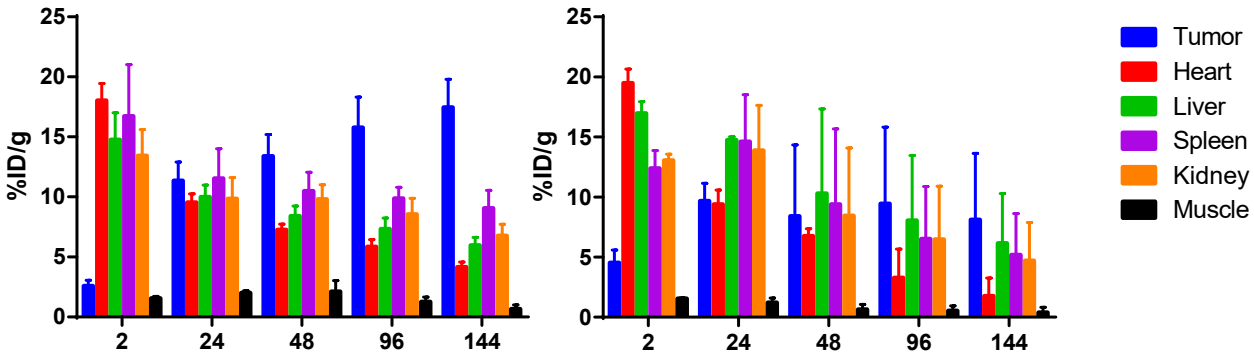

Figure 1 – Distribution of ^{111}In-DTPA-5F9 (left) and ^{111}In-DTPA-TAK-264 (right) in mice bearing HEK-293 GCC#2 subcutaneous tumors.

*Percentage ID/g data are presented as mean ± standard deviations. n = 3-4 for all time points.

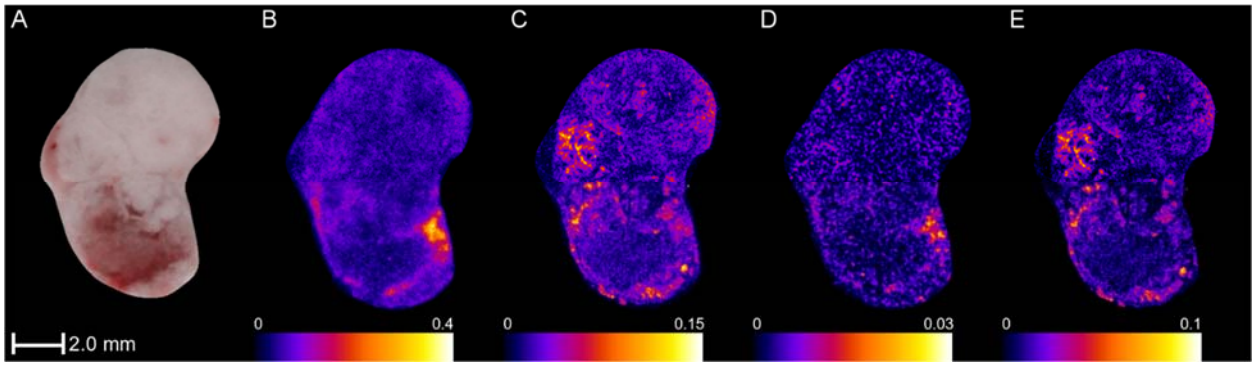

Figure 2 – Representative HEK-293 GCC#2 tumor sections showing the subtraction technique used to compensate for the presence of long-lived contaminants in the ^{111}In labeled ADC. Voxel sizes for all reconstructions are 0.025 x 0.025 x 0.025mm. Images are displayed for qualitative review in units of photostimulated luminescence (PSL). Images show the section's white light image (A), ^{111}In signal (B), Total (^{3}H+contaminants) signal (C), Contaminant only signal (D) and the isolated ^{3}H signal (E)

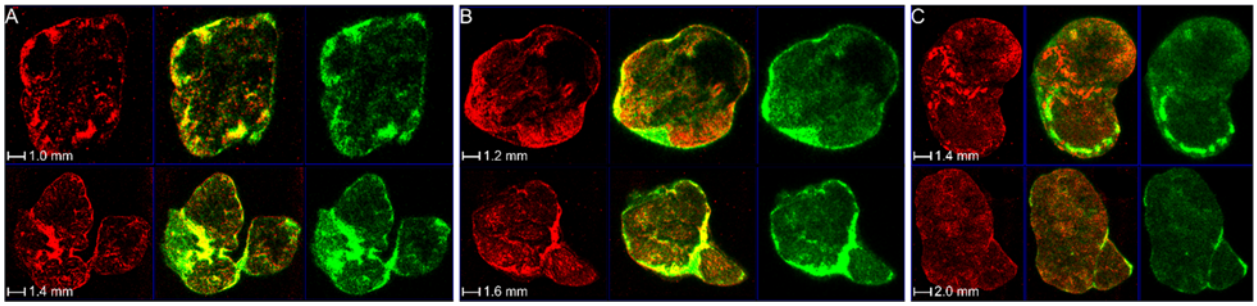

Figure 3 – Representative sections of HEK-293 GCC#2 (top) and HEK-293 (bottom) tumors excised at 1h (A), 24h (B) and 96h (C) post tracer injection. Voxel sizes for all reconstructions are 0.025 x 0.025 x 0.025mm. For each tumor section, the ^{3}H signal is in red, the ^{111}In signal in green and the co-registration of both signals is in yellow. Strikingly, the image of the HEK-293 GCC#2 at 24h shows the initial diffusion of the drug conjugate away from the antibody accumulation site and deeper into the tumor.

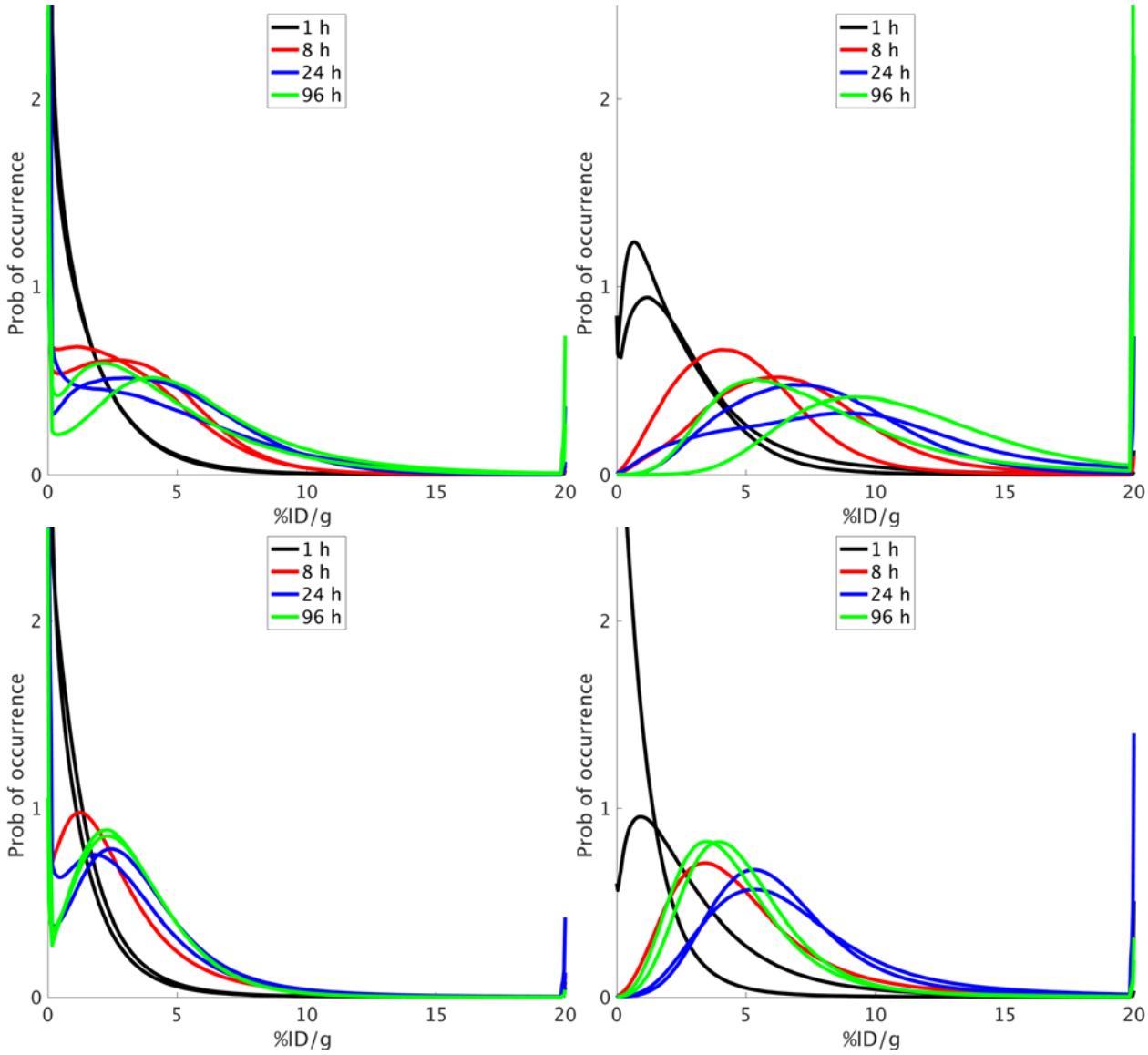

Figure 4 - Distribution of voxel %ID/g values of ^{3}H (A & C) and ^{111}In (B & D) at hours 1 (black), 8 (red), 24 (blue), and 96 (green) hours. Each group contains two animals hence two lines per color.

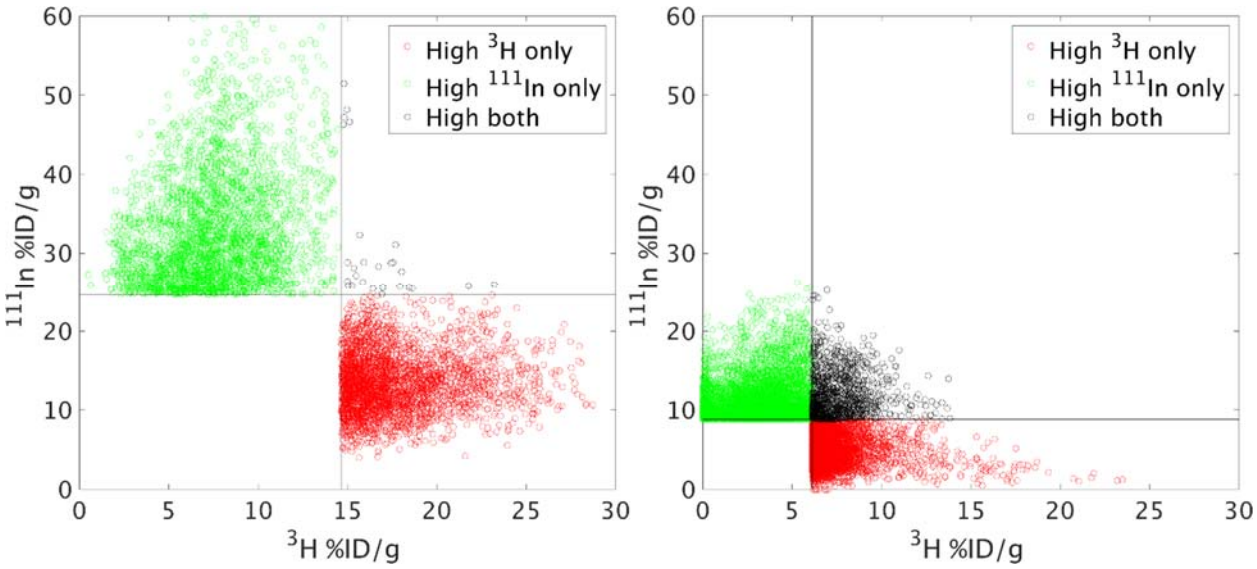

Figure 5 - Co-localization analysis of the top 3% of highest intensity voxels for GCC-positive (left) and GCC-negative (right). Voxels with high indium (antibody, green), tritium (MMAE, red) or both (black) signals are shown.

Supplementary Materials

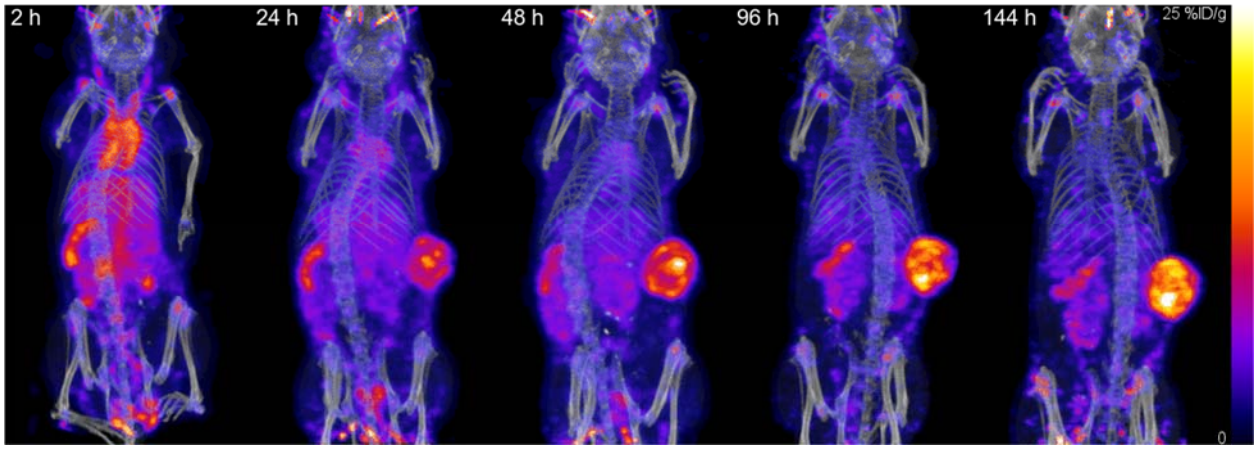

Supplementary Figure 1. Time series of maximum intensity projections of a mouse with a subcutaneous HEK-293 GCC#2 tumor injected with ^{111}In-DTPA-5F9

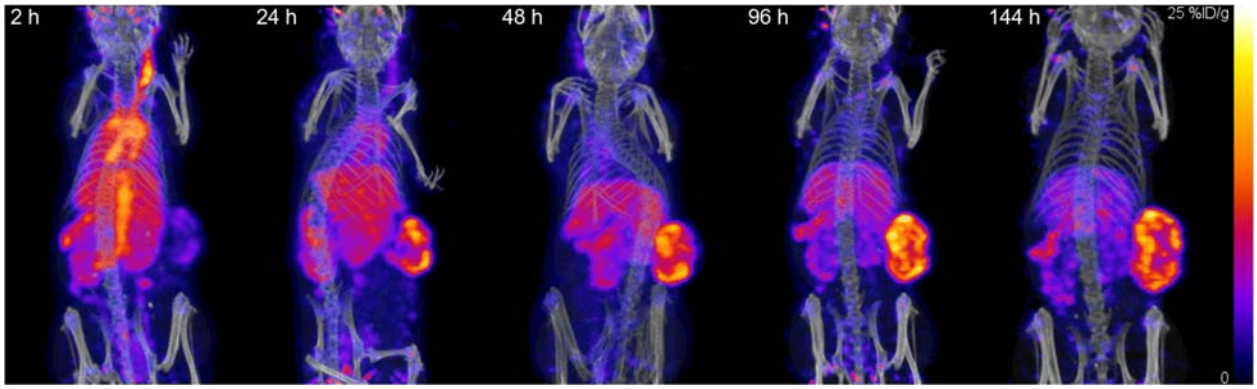

Supplementary Figure 2. Time series of maximum intensity projections of a mouse with a subcutaneous HEK-293 GCC#2 tumor injected with ^{111}In-TAK-264

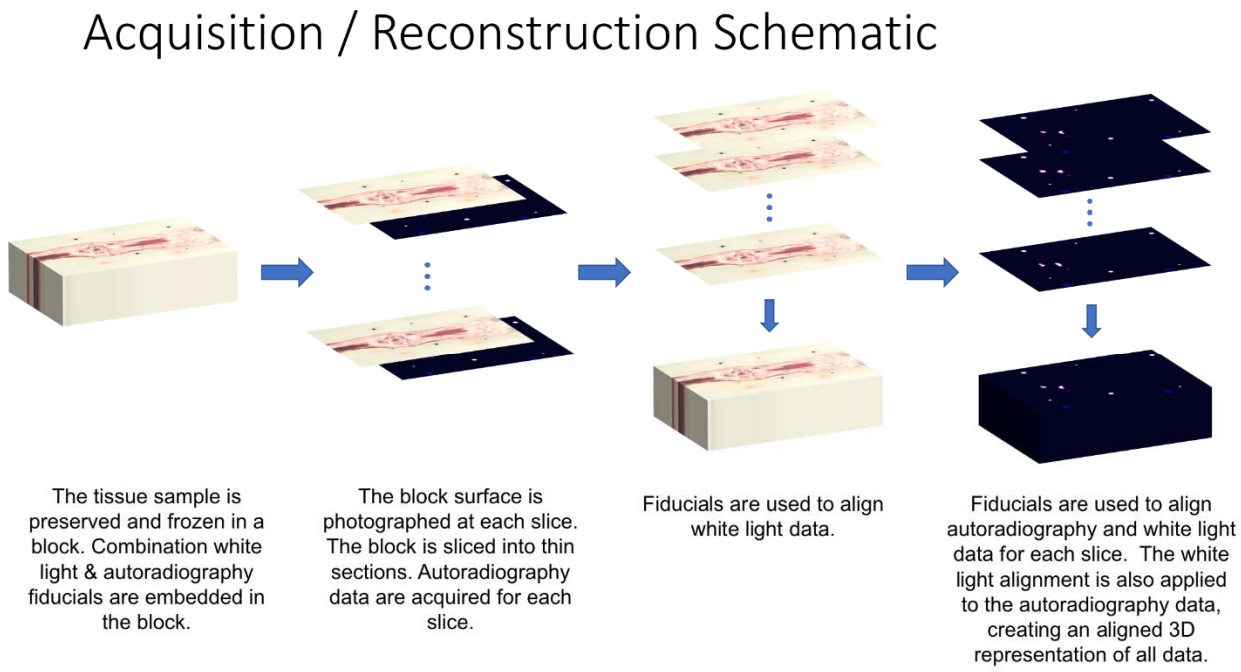

Supplementary Figure 3. Schematic demonstrating the methodology for section signal acquisition and reconstruction of the sections into an aligned 3D representation

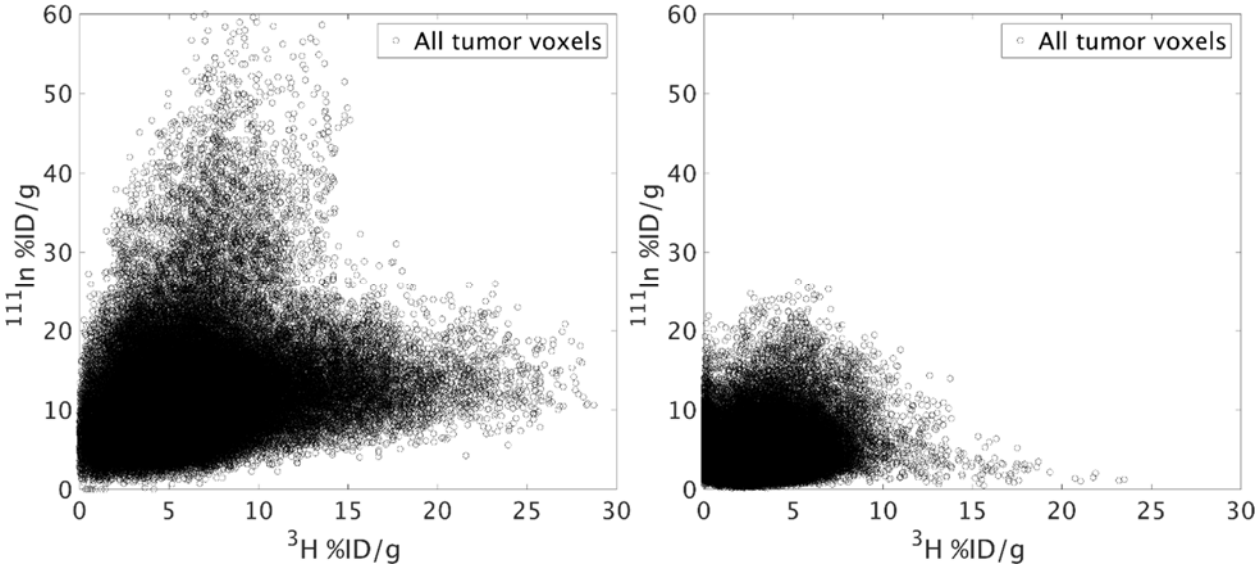

Supplementary Figure 4. Co-localization analysis of all the data from both tumors' datasets without removal of the lower intensity pixels

Supplementary Movie 1. Maximum intensity projections of antigen positive and negative tumors collect 96h post injection.